Critical Role of Structural Water for Enhanced Li⁺ Insertion Kinetics in Crystalline Tungsten Oxides

Focus Issue in Honor of Professor John B. Goodenough: A Centenarian Milestone

James B. Mitchell,[1] Ruocun Wang,[1] Jesse S. Ko,[2] Jeffrey W. Long,[3] & Veronica Augustyn[1,z,*]

[1]*Department of Materials Science and Engineering,* North Carolina State University, Raleigh, North Carolina
[2]*Research and Exploratory Development Department*, Johns Hopkins University Applied Physics Laboratory, Laurel, Maryland
[3]*Surface Chemistry Branch*, U.S. Naval Research Laboratory, Washington, D.C.

[z] Corresponding Author, e-mail address: vaugust@ncsu.edu

Abstract Text

Electrochemical ion insertion into transition metal oxides forms the foundation of several energy technologies. Transition metal oxides can exhibit sluggish ion transport and/or phase-transformation kinetics during ion insertion that can limit their performance at high rates (< 10 min). In this study, we investigate the role of structural water in transition metal oxides during Li^+ insertion using staircase potentiostatic electrochemical impedance spectroscopy (SPEIS) and electrochemical quartz crystal microbalance (EQCM) analysis of $WO_3 \cdot H_2O$ and WO_3 thin-film electrodes. Overall, the presence of structural water in $WO_3 \bullet H_2O$ improves

Li^+ insertion kinetics compared to WO_3 and leads to a less potential-dependent insertion process. *Operando* electrogravimetry and 3D Bode impedance analyses of nanostructured films reveal that the presence of structural water promotes charge accommodation without significant co-insertion of solvent, leading to our hypothesis that the electrochemically induced structural transitions of WO_3 hinder the electrode response at faster timescales (< 10 min). Designing layered materials with confined fluids that exhibit less structural transitions may lead to more versatile ion-insertion hosts for next-generation electrochemical technologies.

Introduction

Electrochemical ion insertion from a liquid electrolyte into a solid-state host forms the basis of lithium-ion batteries[1] and electrochromic windows.[2] This general mechanism is also encountered in such emerging technologies as electrochemical desalination, elemental recovery,[3] neuromorphic computing,[4,5] and tunable catalysts.[6] In both established and emerging applications of electrochemical ion insertion, it is desirable, and often necessary, to optimize the insertion kinetics. The primary kinetic steps associated with electrochemical ion insertion into a solid-state host are ion migration in the electrolyte, charge transfer at the solid/liquid interface (including ion desolvation and electron injection), ion diffusion and electron transport in the solid-state host, and (in some cases) solid-state phase transformation. To obtain fast insertion kinetics, the energy barriers associated with these kinetic processes need to be minimized or eliminated.

Investigation of the insertion properties of transition metal oxides include pioneering contributions by Prof. John B. Goodneough.[7] Transition metal oxides exhibit high redox potentials and can typically accommodate at least 1 e^-/ion per transition metal, which gives rise to relatively high specific capacities.[8,9] In terms of insertion rate, transition metal oxides exhibit kinetic limitations from solid-state transport, phase transformations, and/or electron transport.[10,11] As a result, there is a significant interest in understanding structural features of materials that enable fast ion-insertion reactions. One of these features is the presence of structural water, which has been hypothesized to decrease activation barriers for interfacial charge transfer, enable fast ion diffusion in the solid state, and decrease nucleation barriers during phase transformations.[9,12–14]

To understand the effects of structural water on electrochemical ion insertion in transition metal oxides, we recently studied electrochemical proton insertion into crystalline tungsten oxide hydrates ($WO_3 \cdot nH_2O$, n = 1, 2) and compared their response to anhydrous WO_3, a well-known proton insertion host. We observed that $WO_3 \cdot nH_2O$ exhibit higher capacity retention

and electrochemical reversibility compared to WO_3 at fast rates (cyclic voltammetry sweep rates > 20 mV s^{-1}, corresponding to charging times < 1 min).[15] *Operando* atomic force microscopy dilatometry showed notable differences in the deformation of $WO_3 \cdot 2H_2O$ vs. WO_3 upon proton insertion: $WO_3 \cdot 2H_2O$ showed lower deformation and hysteresis between the insertion / de-insertion processes and a smaller dependence of the deformation on the cyclic voltammetry sweep rate.[16] We also compared the kinetics of the structural transformations of $WO_3 \cdot 2H_2O$ and WO_3 during proton insertion using *operando* synchrotron X-ray diffraction (XRD). We found that the structural transformation of $WO_3 \cdot 2H_2O$ is more kinetically facile than in WO_3.[12] These findings indicate that the primary benefit of structural water during proton insertion into $WO_3 \cdot nH_2O$ is to minimize structural transitions that accompany proton insertion.

The purpose of this study was to elucidate the kinetics of Li^+ insertion into $WO_3 \cdot nH_2O$ as compared to WO_3. We investigated Li^+ insertion in non-aqueous electrolytes because tungsten oxides are not stable at neutral pH.[17] Moreover, Li^+ insertion from a non-aqueous electrolyte can occur over a broader potential window, not limited by the hydrogen evolution reaction as in the case of proton insertion at low pH. This renders it more promising for technological application. First, we sought to determine whether the kinetic trends observed for proton insertion would apply for non-aqueous Li^+ insertion. Second, we aimed to elucidate the effects of structural water on interfacial charge transfer by correlating electrogravimetric and impedance responses. There are prior reports on the electrogravimetric and impedance responses of crystalline and amorphous WO_3 thin film electrodes,[18–20] but they did not focus on understanding the role of structural water during ion insertion in WO_3.

We compared electrochemical Li^+ insertion kinetics into $WO_3 \cdot H_2O$ and WO_3 using electrochemical quartz crystal microbalance (EQCM) and staircase potentiostatic electrochemical impedance spectroscopy (SPEIS)[21,22] measurements. The techniques were

4

used to understand the electrode mass change and its correlation to the frequency-dependence of Li^+ insertion. EQCM shows that both oxides exhibit negligible solvent co-insertion. This is significant because the observed kinetic differences due to the presence of structural water are thus not due to lowered activation barriers for interfacial charge transfer. The nanostructured thin films in this study limit kinetic losses due to ion diffusion and electron transport in the solid-state. Therefore, these studies indicate that structural water leads to more facile structural transformations during Li^+ insertion, enabling more Li^+ storage across a wider potential and frequency range in $WO_3 \bullet H_2O$ compared to WO_3. Overall, our results demonstrate the importance of minimizing the kinetic barriers associated with the nucleation of new solid-state phases during Li^+ insertion, and how the deliberate incorporation of structural water is one design strategy to accomplish that goal.

Experimental

Materials Synthesis – $WO_3 \cdot 2H_2O$ was electrodeposited via an electrochemically assisted acid-precipitation process, as described previously.[23,24] Briefly, the films were electrodeposited onto 5 MHz polished Au quartz crystals (Phillip Technologies, SC, USA) from a solution of 12 mmol L^{-1} Na_2WO_4 (Sigma-Aldrich) in deionized water at 70°C.[23] Once at temperature, concentrated H_2SO_4 (ACS Grade, Fisher Scientific) was added to the stirring solution to achieve a final concentration of 0.5 mol L^{-1} H_2SO_4. The Au-deposited quartz crystal served as the working electrode, platinum wire as the counter electrode (99.997%, Alfa Aesar), and Ag/AgCl in a saturated KCl solution as the reference electrode (Pine Instruments). The heated solution was used for electrodeposition without cooling. Films were electrodeposited using cyclic voltammetry at 100 mV s^{-1} between -0.2 and 1.0 V vs. Ag/AgCl for 3 h. Subsequently, the films were removed from the electrodeposition solution and aged in 0.5 mol L^{-1} H_2SO_4 for 24 h at room temperature.[24] The electrodeposited film mass was determined from the shift in resonance frequency of the quartz crystal in air before and after deposition. The mass was calculated using the Sauerbrey equation:[25]

$$\Delta F = -C_f * \Delta m \tag{1}$$

where ΔF is the shift in the resonance frequency (5 MHz) of the quartz crystal, C_f is the sensitivity factor ($C_{f, dry\ air}$ = 56.6 Hz g^{-1} cm^2), and Δm is the change in mass. Orthorhombic $WO_3 \bullet H_2O$ was obtained by heat treatment of the electrodeposited films at 120 °C in air for 12 h, and anhydrous monoclinic WO_3 by heat treatment in argon at 350 °C for 12 h. The inert atmosphere condition was necessary to prevent oxidation of the adhesion layer between the quartz crystal and Au pad at elevated temperatures.

Physical Characterization – Film morphology was characterized using a field emission scanning electron microscope (SEM; FEI Verios 460L). Structural characterization was obtained via Raman spectroscopy using a WiTEC alpha300R confocal Raman microscope with a laser wavelength of 532 nm, 100x lens objective and 6 s integration time. Reported spectra were averaged over four scans.

Electrochemical Characterization – Films were characterized in an argon-filled glovebox (< 1 ppm O_2, H_2O) in a three-electrode cell with Li-metal counter and reference electrodes (99.9%, Aldrich). The electrochemical cell geometry was controlled to maintain similar uncompensated solution resistance during measurements. The electrolyte was 1 mol L^{-1} LiClO$_4$ (electrochemical grade, Aldrich) in propylene carbonate (Sigma Aldrich). All experiments were conducted at room temperature (21 ± 1 °C) using a BioLogic VMP3 potentiostat.

Electrodeposited films were first conditioned at 10 mV s^{-1} for 10 cycles between 2.0 – 3.5 V vs. Li/Li$^+$. Cyclic voltammetry was conducted from 1 – 100 mV s^{-1} between 1.8 and 3.5 V vs. Li/Li$^+$ to obtain *operando* electrogravimetry as a function of potential. Films were subjected to 10 cycles at each sweep rate to obtain statistical data. Electrogravimetric data were collected using a quartz crystal microbalance (SRS QCM 200) with a 100-ms frequency counter (0.1 Hz resolution) for the faster sweep rates (≥ 20 mV s^{-1}) and 1 s acquisition (1 Hz resolution) for the slower sweep rates (≤ 10 mV s^{-1}). The recorded frequency shift (ΔF) was

related to the mass change (Δm) at the electrode-electrolyte interface using Equation 1. C_f in solution was obtained by determining ΔF during a well-known electrochemical reaction.[33] In this work, C_f was determined using the electrodeposition of Ag:

$$Ag^+ + e^- \rightarrow Ag_{(s)} \tag{2}$$

Ag was electrodeposited using chronopotentiometry for 3 min with current densities of 5, 10, 20, and 50 μA cm^{-2} from a solution of 10 mmol L^{-1} $AgClO_4$ (anhydrous, Alfa Aesar) in a supporting electrolyte of 100 mmol L^{-1} tetrabutylammonium perchlorate (electrochemical grade, Alfa Aesar) in propylene carbonate with Ag wire (99.9%, Alfa Aesar) counter and pseudoreference electrodes. The mass of Ag was calculated by applying Faraday's law, assuming 100% faradaic efficiency. C_f (4.2 ± 0.4 · 10^7 Hz g^{-1}, 95% confidence) was obtained from the slope of the linear regression of ΔF vs. Δm (**Figure S1**). A Matlab code was used to perform all EQCM data processing.[26]

Staircase potential electrochemical impedance spectroscopy (SPEIS) experiments were conducted with 50-mV resolution between 1.8 and 3.5 V vs. Li/Li$^+$. The electrochemical cell was the same as described for EQCM experiments. The electrode was held at each potential to equilibrate for 10 min before taking the impedance spectrum from 200 kHz – 10 mHz with a sinusoidal voltage amplitude of 10 mV.

Results and Discussion

To investigate the effects of structural water on Li$^+$ insertion in crystalline tungsten oxides, we explored the electrochemical behavior of electrodeposited thin films of each material (monoclinic $WO_3 \cdot 2H_2O$ and WO_3; orthorhombic $WO_3 \cdot H_2O$, **Figure S2**). The crystal structure of each material was confirmed via Raman spectroscopy (**Figure S3**). Since $WO_3 \cdot 2H_2O$ transforms into $WO_3 \cdot H_2O$ in a non-aqueous electrolyte,[27] only $WO_3 \cdot H_2O$ and WO_3 thin films were used for subsequent electrochemical analysis to investigate the role of structural water during Li$^+$ insertion. Electrochemical deposition of $WO_3 \cdot nH_2O$ results in a

porous, nanostructured thin film with plate-like morphology. Thermal dehydration and conversion of $WO_3 \cdot H_2O$ into WO_3 yields similar film morphologies with modest particle sintering (**Figure S4**). The particle size increased from 82 ± 13 nm in $WO_3 \cdot H_2O$ to 167 ± 27 nm for WO_3. However, since we controlled the solution resistance between experiments by maintaining similar electrochemical cell geometry, the similar series resistances (R_s) between WO_3 and $WO_3 \cdot H_2O$ films indicate no significant changes to the contact between film and substrate after thermal treatment (**Figure S5**).

In $WO_3 \cdot H_2O$ and WO_3, Li^+ insertion (limited to $x < 1$) involves concomitant electron transfer and reduction of the host metal oxide.[28,29] Cyclic voltammograms (CVs) of $WO_3 \cdot H_2O$ and WO_3 from $1 - 100$ mV s^{-1} (**Figure 1a,b**) show smaller peak-to-peak separation (150 mV vs. 300 mV at 1 mV s^{-1}) and better rate capability for $WO_3 \cdot H_2O$, similar to our previous findings for aqueous proton insertion.[12,15] Li^+ insertion into $WO_3 \cdot H_2O$ occurs over a wider potential range with less potential dependence than in WO_3. This observation is also in line with our previous report of proton insertion into $WO_3 \cdot 2H_2O$ vs. WO_3.[15]

The combination of small particle sizes and the nanoporous nature of the films yields short diffusion distances which help minimize kinetic losses that would otherwise be associated with solid-state Li^+ diffusion. We can also estimate the diffusion distance (x) based on the reported diffusion coefficient for Li^+ in polycrystalline WO_3 films at room temperature ($D_{Li} \sim 10^{-10}$ cm^2 s^{-1})[30] and assuming that $x \sim (2Dt)^{0.5}$. At 1 mV s^{-1}, $x \sim 6$ μm and at 100 mV s^{-1}, $x \sim 600$ nm. Because the average particle sizes from SEM are less than the estimated diffusion distances at these rates for both materials, we hypothesize that differences in Li^+ intercalation kinetics are not due to differences in Li^+ solid-state mass transport. We determined the relationship between cyclic voltammetry current and sweep rate ($i \sim av^b$), and found that between 1 and 10 mV s^{-1} the b-values for $WO_3 \cdot H_2O$ and WO_3 were, respectively,

0.90 and 0.85 (**Figure S6)**. This response indicates that Li^+ insertion into thin films of both materials is not limited by semi-infinite diffusion of Li^+ in the solid state or liquid electrolyte (b = 0.5) at these sweep rates. Given the thin-film nature of the electrodes, non-mass transfer rate limitations are likely, such as from the surface reaction, Ohmic drop across the oxide film, or activation barrier associated with the nucleation of a new solid-state phase.[31] Both WO_3 and $WO_3 \bullet H_2O$ are semiconductors, with band gaps of ~ 2.6 eV[32] and 2.5 eV[33], respectively.

Assuming these are intrinsic semiconductors, the electrical conductivity of the as-synthesized films should be similar, leading to similar Ohmic drops upon the initial Li^+ insertion. During cation insertion, tungsten oxides (including hydrates) undergo a semiconductor-to-metal transition when x ~ > 0.2.[32] Given these similarities in the electronic structure, including changes during ion insertion, we do not expect electronic conductivity to lead to the kinetic differences observed between WO_3 and $WO_3 \bullet H_2O$.

At the slowest sweep rates tested (1 mV s^{-1}, ~ 30 min charge / discharge), $WO_3 \cdot H_2O$ exhibits higher Li^+ charge-storage capacity (300 C g^{-1}, ~ 0.75 Li:W) than WO_3 (175 C g^{-1}, ~ 0.4 Li:W). While WO_3 possesses a higher theoretical specific capacity than $WO_3 \cdot H_2O$, the initial conditioning process at 10 mV s^{-1} leads to more irreversible capacity loss in WO_3 than $WO_3 \cdot H_2O$ (**Figure S7**). Wen et al.[34] revealed irreversible ion trapping as a possible degradation pathway in WO_3 when Li:WO_3 > 0.5. This is a feasible explanation of the faster capacity decline in WO_3 compared to $WO_3 \cdot H_2O$ during the conditioning cycles (**Figure S7c**). Additionally, $WO_3 \cdot H_2O$ exhibits lower efficiencies (~89% vs. ~99% at 1 mV s^{-1}) than WO_3 but has highly reversible charge storage (> 99%) at faster rates (> 10 mV s^{-1}, < 0.5 Li:$WO_3 \cdot H_2O$). This suggests that irreversible ion trapping may also explain the lower CE and faster capacity degradation for $WO_3 \cdot H_2O$ at the slowest rates (< 10 mV s^{-1}). However, the presence of structural water leads to enhanced capacity retention compared to WO_3 at the faster rates (> 10 mV s^{-1}) where charge storage is highly reversible. Our findings of the kinetic differences between $WO_3 \cdot H_2O$ and WO_3 during Li^+ insertion are in-line with those of Judeinstein and

Livage, who studied the electrochromic response of tungsten oxide films with varying structural water content in a non-aqueous Li^+ electrolyte.[35]
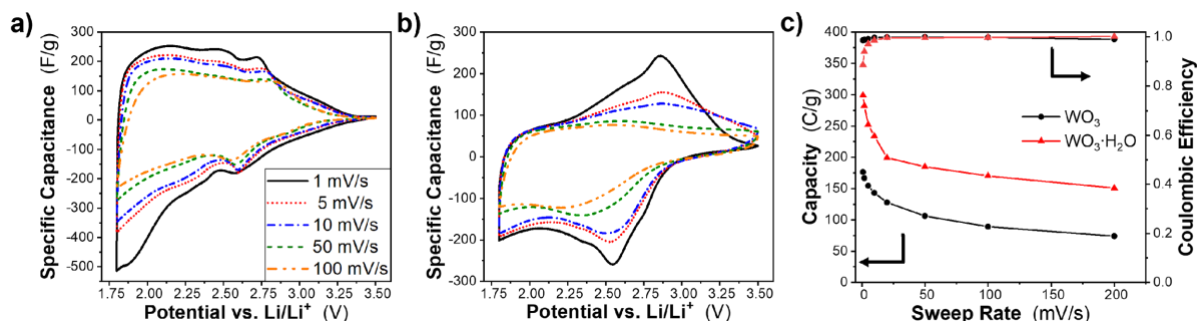
**Figure 1: Cyclic Voltammetry of Electrodeposited Tungsten Oxide Films |** CVs from 1 – 100 mV s^{-1} of $WO_3 \cdot H_2O$ (a) and WO_3 (b) in 1 M $LiClO_4$ in PC. (c) Capacity retention and Coulombic efficiency as a function of sweep rate.

To understand the mechanism of Li^+ insertion into $WO_3 \cdot H_2O$ and the reason for the kinetic difference with WO_3, we performed *operando* electrogravimetry with EQCM and SPEIS. These techniques were selected because they enabled a systematic study of the effects of structural water through a detailed understanding of the Li^+ charge transfer process at the electrochemical interface.

Figure 2 shows the representative electrogravimetric behavior (Δm vs. E) of $WO_3 \cdot H_2O$ and WO_3 at 10 and 100 mV s^{-1} (corresponding to charge / discharge times of 3 min and 18 s, respectively). At 10 mV s^{-1}, in the cathodic cycle $WO_3 \cdot H_2O$ exhibits little mass change until ~ 3 V, when the current begins to decrease (**Figure 2a**). Decreasing potential leads to a further increase in Δm, as expected for an insertion reaction. Between ~2.8 and 1.8 V, the potential dependence of Δm appears almost linear. During the anodic (Li^+ de-insertion) scan, Δm begins to decrease at ~ 1.9 V, slightly delayed from the 1.8 V cathodic turnover potential. There is

nearly constant hysteresis in the gravimetric response (~260 ± 40 µg) across the scanned potential window between insertion (discharge) and de-insertion (charge), except at the highest potentials where limited charge storage takes place (Δm < 0.25 µg) and at the cathodic turnover potential. The overall Δm upon Li^+ insertion into $WO_3 \cdot H_2O$ at 10 mV s^{-1} is 3.5 µg (22 mg g^{-1} $WO_3 \cdot H_2O$) with a capacity of ~ 230 C g^{-1}. In WO_3, there are two important differences in the electrogravimetric response: 1) Δm has distinct regions before, during, and after the current peaks, and 2) the hysteresis of Δm also changes as a function of potential, with the largest gravimetric hysteresis (563 ± 13 µg) occurring when Δm < 1 µg, which is within the potential region of the redox peaks (**Figure 2b**). The overall Δm upon Li^+ insertion into WO_3 at 10 mV s^{-1} is 1.8 µg (18 mg g^{-1} WO_3) for a capacity of ~ 160 C g^{-1}. Upon a ten-fold increase of the sweep rate, both materials exhibit increased polarization that leads to more delayed decrease in Δm upon sweep reversal and increased hysteresis of Δm (**Figure 2c,d**). In $WO_3 \cdot H_2O$, Δm continues to increase until ~ 2.15 V at 100 mV s^{-1} (vs. 1.86 V at 10 mV s^{-1}) in the anodic cycle. In comparing the response of $WO_3 \cdot H_2O$ and WO_3 at 100 mV s^{-1}, WO_3 appears more kinetically reversible. However, at this rate, Li^+ insertion into WO_3 is half the value of $WO_3 \cdot H_2O$ (~ 100 C g^{-1} and Δm < 1 µg in WO_3 vs. ~ 200 C g^{-1} and Δm > 3 µg in $WO_3 \cdot H_2O$). These differences highlight the ability for $WO_3 \cdot H_2O$ to accommodate additional charge density compared to WO_3, especially at fast rates (t < 1 min).
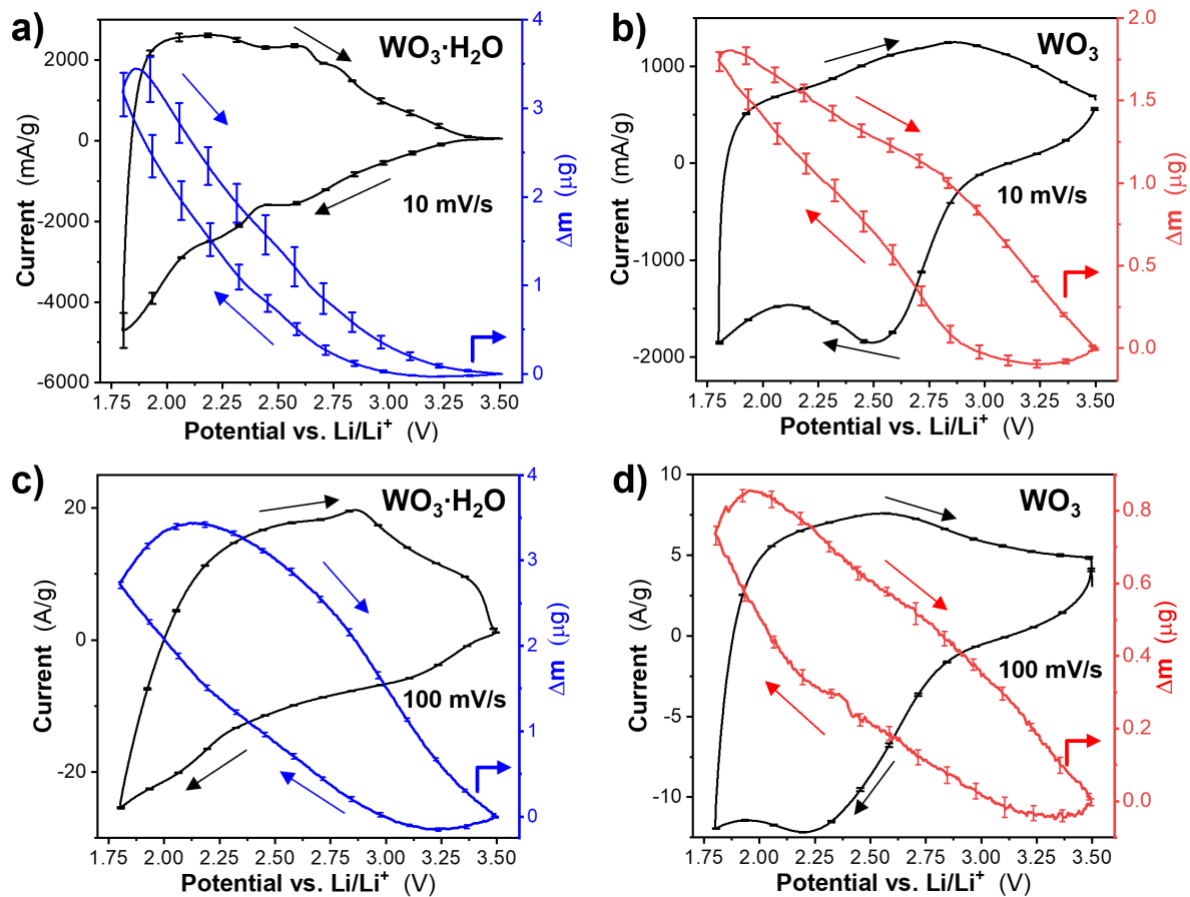
Figure 2: Dynamic Mass Change during Li⁺ Insertion into WO₃•H₂O and WO₃ | Potential-dependent electrogravimetric responses overlaid on the voltammetric responses for $WO_3 \cdot H_2O$ (a, c) and WO_3 (b, d) electrochemically cycled in a non-aqueous $LiClO_4$ electrolyte at 10 (a, b) and 100 (c, d) mV s⁻¹. Massograms (right *y*-axis, blue / red) represent the change in mass (Δm) of the electrodeposited films as a function of potential. Voltammograms (left *y*-axis) are the current response as a function of potential. All curves are represented as the average ± standard deviation for 10 cycles.

The nature of the inserted species (Li⁺ vs. Li⁺ solvated by n PC molecules) can be obtained from the slope of Δm vs. integrated charge (Q), also known as the mass-to-charge ratio (MCR; **Figure 3**). This analysis was used previously to understand the solvation environment of electrosorbed and inserted species on nanoporous carbons,[36] graphite,[37] and

2D MXene.[38] The apparent molecular mass (M'_w) of species can be calculated from the slope of a linear region in Δm vs. Q:[36]

$$M'_w = zF\left(\frac{m}{Q}\right) \tag{3}$$

where z is the number of electrons and F is Faraday's constant. The calculated M'_w can be used to determine the solvation number (n) of Li$^+$, that is, the number of PC molecules associated with each Li$^+$ at the electrochemical interface:

$$n = \frac{M'_w - M_{w\,(Li)}}{M_{w\,(PC)}} \tag{4}$$

where $M_{w\,(Li)}$ is the molecular weight of Li$^+$ and $M_{w\,(PC)}$ is the molecular weight of propylene carbonate. **Table S1** lists values of M'_w and n for both materials and sweep rates.
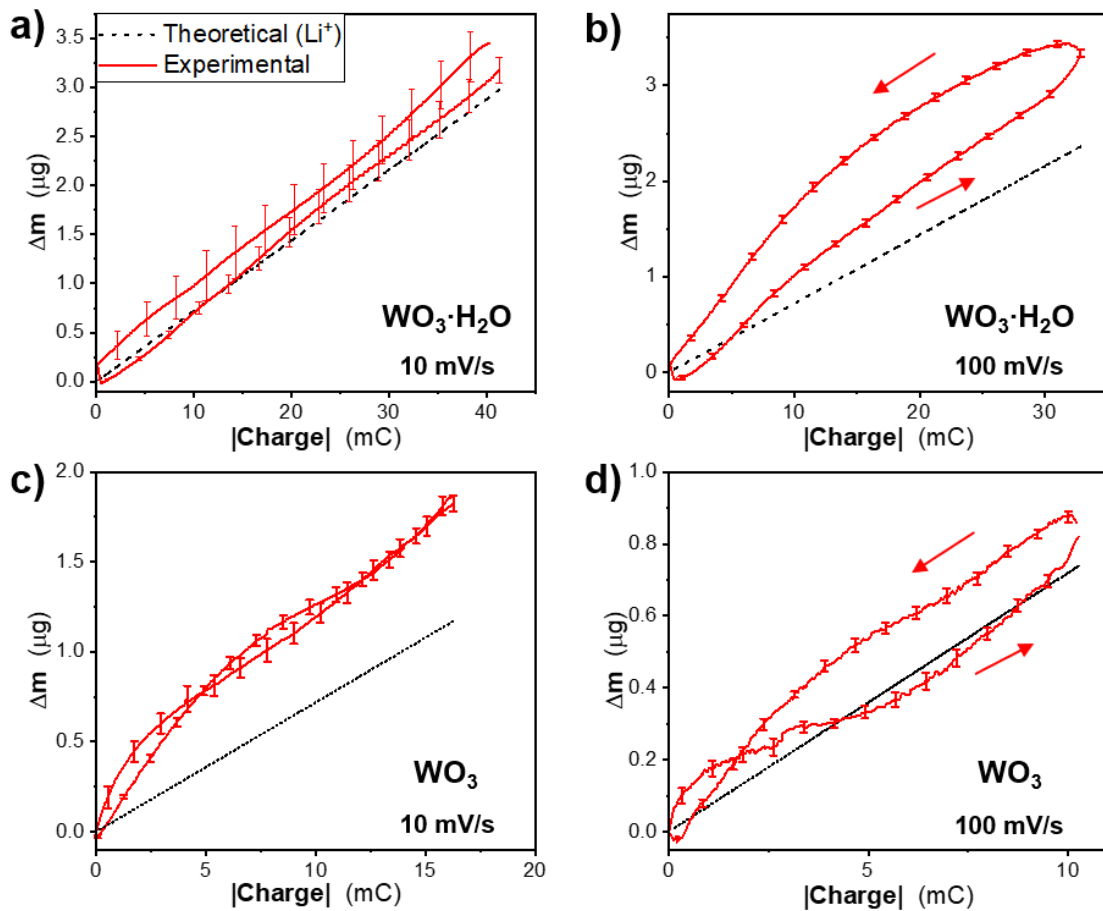
Figure 3: Mass Change vs. Charge in WO₃•H₂O and WO₃ | Electrogravimetric responses as

a function of integrated charge for $WO_3 \cdot H_2O$ (a, b) and WO_3 (c, d) at 10 (a, c) and 100 (b, d)

mV s^{-1}. The absolute value of the integrated charge is included to highlight the hysteresis

between the forward (cathodic) and reverse (anodic) scans. The black dashed lines for each

plot represent the calculated mass change for desolvated Li$^+$ (de)insertion. The red curves

represent the experimentally recorded data and are represented as the average ± standard

deviation for 10 cycles.

At 10 mV s^{-1}, Δm vs. Q for $WO_3 \cdot H_2O$ exhibits excellent agreement with the calculated Δm

for desolvated Li$^+$ insertion (black dotted line, **Figure 3a**). This means that at 10 mV s^{-1}, over

the entire extent of Q, Li$^+$ inserts without a solvation shell into $WO_3 \cdot H_2O$. At 100 mV s^{-1}, there

are slight deviations from the calculated Δm, particularly at low Q (< 10 mC) (**Figure 3b**). The

PC-solvation number of the intercalating species at the electrochemical interface is less than

1 (**Table S1**). While we cannot definitively exclude some solvent co-insertion in $WO_3 \cdot H_2O$ at

higher sweep rates, it is possible that the changes are primarily due to changes in electrolyte

flux within electrode pores. According to Levi et al., the electrogravimetric response of porous

electrodes can contain contributions from ion / solvent co-insertion into the electrode as well

as solvent flux within the electrode pores.[39] However, we can conclude that there is no

significant solvent co-insertion in $WO_3 \cdot H_2O$ across all sweep rates. This is important because

it means that $WO_3 \cdot H_2O$ maintains relatively high insertion capacity at 100 mV s^{-1} (206 C g^{-1};

0.5 Li$^+$/W) with interfacial Li$^+$ desolvation. While Li$^+$ desolvation can be a major contributor to

the activation barrier for interfacial charge transfer,[40] it does not appear to play a significant

role in the kinetic response of $WO_3 \cdot H_2O$ at the timescales probed by our study. The behavior

of $WO_3 \cdot H_2O$ is thus in contrast to hydrated transition metal oxides such as V_2O_5 xerogels,

which showed a sweep-rate dependent solvation of inserting Li^+.[41]

WO$_3$ exhibits larger deviations from the calculated Δm for Li^+ insertion than WO$_3\cdot$H$_2$O

(**Figure 3c, d**), but overall, similar trends are observed. The deviations occur mainly at lower

Q ($|Q| < 5$ mC) (**Table S1**) but still indicate relatively minimal amount of solvent co-insertion (n

< 0.02 per WO$_3$). Since, to the best of our knowledge, there are no reports of solvent co-

insertion into monoclinic WO$_3$,[42] we assume that the deviations from the calculated MCR are

due to changes in the viscoelastic properties at the electrode-electrolyte interface caused by

electrolyte flux. At 100 mV s^{-1} (**Figure 3d**), WO$_3$ displays similar behavior as WO$_3\cdot$H$_2$O.

However, the magnitude of Δm is quite low due to the limited Li^+ insertion capacity (102 C g^{-1};

0.25 Li^+/W).

Overall, the electrogravimetric study reveals that neither WO$_3\cdot$H$_2$O nor WO$_3$ exhibit

solvent co-insertion during Li^+ insertion. This is significant in the case of layered WO$_3\cdot$H$_2$O:

despite an interlayer spacing of 5.36 Å, the interlayer-confined structural water appears to

prevent solvent co-insertion. Therefore, we hypothesize that Li^+ insertion into WO$_3\cdot$H$_2$O is

faster than in WO$_3$ due to more facile structural transformation, as we previously observed

during H^+ (de)insertion.[12,16]

To complement the electrogravimetric study and elucidate the kinetic differences of the

electrochemically induced structural transformations, we performed EIS because it offers

insights into the kinetics of Li^+ insertion in WO$_3\cdot$H$_2$O and WO$_3$ based on the frequency

response to an alternating voltage perturbation. In particular, 3-D Bode plot representations

provide additional mechanistic insights regarding the temporal/frequency responses of these

potential-dependent processes.[21,22] Plotting the frequency-dependent data as a function of

potential provides a comprehensive representation of the electrode kinetics.[22] In the low-

frequency range (0.01 – 1 Hz), we used the method described by Taberna et al.[43] to represent

the impedance response of both materials as a simple circuit composed of a frequency-dependent resistor and capacitor in series.[21] The real and imaginary components of the frequency-dependent capacitance, $C'(\omega)$ and $C''(\omega)$, respectively, can be calculated using:[21,44]

$$C'(\omega) = \frac{-Z''(\omega)}{\omega |Z(\omega)|^2} \tag{5}$$

$$C''(\omega) = \frac{Z'(\omega)}{\omega |Z(\omega)|^2} \tag{6}$$

where $Z'(\omega)$ and $Z''(\omega)$ are the real and imaginary impedance as a function of the angular frequency, ω. C' represents the deliverable or reversible charge at a given frequency,[21,44] and reflects contributions from fast, reversible electrochemical processes.[22] C'' corresponds to energy losses due to irreversible electrochemical processes at the electrode,[43] such as diffusion limitations.[21] Both provide additional insights into the kinetic differences of Li$^+$-charge storage in $WO_3 \cdot H_2O$ and WO_3.

The frequency dependence of C' and C'' for $WO_3 \cdot H_2O$ and WO_3 at six different potentials is shown in the Bode Plots in **Figure 4**. These potentials were chosen to highlight the evolution of the capacitance throughout the potential window. We will first discuss the frequency dependence of C' (Figures 4a and 4b). For both materials, C' goes to zero at higher frequencies as the electrodes transition to a resistive state (**Figure S8**). At lower frequencies, the electrodes transition to a capacitive state. A plateau in C' indicates that the maximum capacitance was reached within the investigated frequency regime. It is thus representative of the characteristic time to obtain the maximum reversible capacitance at each potential.[45] C' is generally greater at all potentials and frequencies in $WO_3 \cdot H_2O$ than WO_3. $WO_3 \cdot H_2O$ exhibits a plateau in C' for each potential as well as the "waterfall" behavior,[21] where C' values gently fall off with increasing frequency (**Figure 4a**). This indicates that $WO_3 \cdot H_2O$ obtains the maximum capacitance within this frequency ($f < \sim 0.1$ Hz) / timescale ($t > 10$ s). Conversely, the behavior of C' in WO_3 is more frequency-dependent (**Figure 4b**). The largest C' occurs at 2.4 V but does not reach the maximum reversible charge storage. This plateau behavior is

obtained in WO_3 electrodes outside of the potential region where the redox peaks occur, indicating that the structural transformations associated with the redox peaks are kinetically limiting the electrochemical response. These results are in line with the cyclic voltammetry data (Figure 1), which shows limited charge storage at fast rates in WO_3 electrodes.
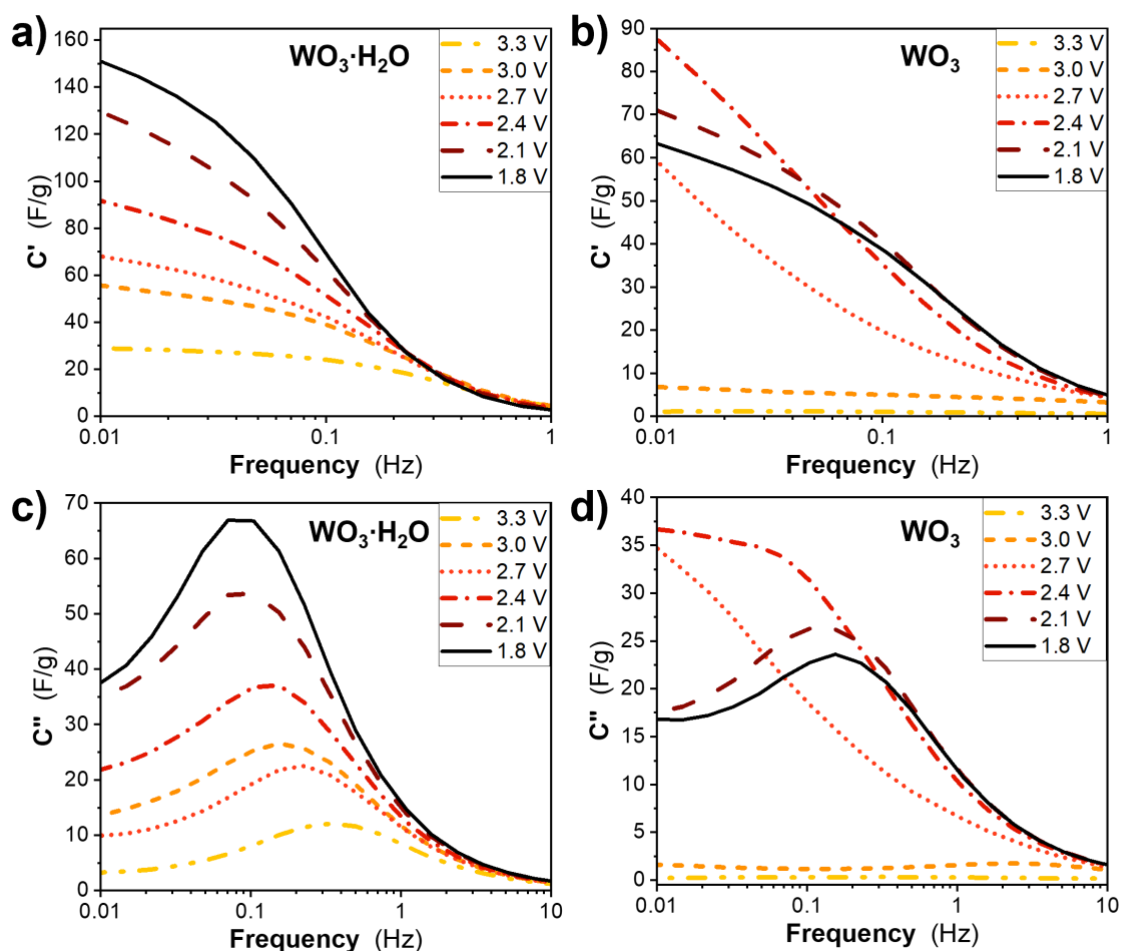
Figure 4: 2D Bode Plots of the Frequency-Dependent Impedance of $WO_3 \cdot H_2O$ and WO_3

| (a, b) Frequency dependence of *C'* for $WO_3 \cdot H_2O$ and WO_3, respectively and (c, d) Frequency dependence of *C''* for $WO_3 \cdot H_2O$ and WO_3, respectively.

The potential-dependent slices at various frequencies help highlight the differences in the charge-storage processes as a function of frequency / rate for the two materials (**Figure S9**).

WO$_3$ exhibits potential-dependent Li$^+$ insertion: significant charge storage occurs in a finite potential region. Therefore, we hypothesize that as the frequency of the applied potential increases, the kinetic limitations of the structural transformations associated with this mechanism inhibit significant Li$^+$ insertion at higher frequencies (**Figure S9d**). In WO$_3$•H$_2$O, the C' vs. potential plot transitions from a linear response with a semi-constant slope throughout the entire potential range to a plateaued maximum reversible capacity. This ideal capacitive behavior at high rates (228 mHz, < 5 s) indicates that charge storage in WO$_3$•H$_2$O is not limited by the electrochemically induced structural transitions caused by Li$^+$ insertion in these timescales. The increasing reversible charge storage as a function of potential reveals a transition from the more potential-dependent Li$^+$ insertion in WO$_3$ to a more potential-independent process in WO$_3$•H$_2$O.

We next discuss the frequency dependence of C'', whose maximum corresponds to the transition point from capacitive to resistive behavior in the model circuit. WO$_3$•H$_2$O exhibits a maximum in C'' at all potentials (**Figure 4c**), consistent with the waterfall behavior of C'. The C'' maxima shift to lower frequencies with decreasing potential, with the biggest change occurring between 3.3 and 2.7 V. These shifts correspond to more sluggish responses, indicating that charge storage kinetics are slower upon further reduction (Li$^+$ insertion). WO$_3$ exhibits more potential dependence for C''. There are negligible dissipation losses at 3.3 V and 3.0 V, consistent with the minimal overall charge storage in this region. At the onset of the cathodic redox peak (~ 2.7 V), C'' increases in magnitude and does not exhibit a maximum in the frequency range used here. Because we do not expect solid-state ion diffusion and electron transport limitations in these thin films (*vide supra*), we ascribe these kinetics limitations to the electrochemically induced phase transformations. This behavior is observed until after the cathodic redox peak, where the C'' response then shifts and the transition from resistive to capacitive behavior is realized within this frequency range. After the major

structural rearrangement occurs, more facile Li^+ insertion processes take place.

The potential dependence of the relaxation time (τ) of $WO_3 \cdot H_2O$ and WO_3 was obtained from the maximum of the frequency-dependence of C'' (**Figure 5**). $WO_3 \cdot H_2O$ exhibits semi-constant τ of < 20 s across the entire potential range. This trend points to fundamentally fast Li^+ insertion kinetics across the entire potential range in $WO_3 \cdot H_2O$. Conversely, WO_3 exhibits highly potential dependent τ values. In the potential range of the WO_3 cathodic redox peak, τ is > 100 s. Since C'' did not reach a maximum in this region, the charge storage processes occur over longer timescales / lower frequencies than what was probed with this experiment. The large increase in τ suggests that the structural transition associated with the nucleation of the tetragonal phase from the insertion of Li^+ into monoclinic WO_3[28,46] is a rate-limiting step. After the cathodic redox peak, τ sharply decreases to similar values as for $WO_3 \cdot H_2O$. The kinetic limitations of these structural transformations in WO_3 clearly limit the overall charge storage within the stable potential range. Charging / discharging at high rates polarizes the electrochemical response of WO_3 and shifts significant Li^+ charge-storage capacity outside of the potential window. Conversely, Li^+ charge storage in $WO_3 \cdot H_2O$ is potential-independent, alluding to the facile structural transitions enabled by its layered, hydrated structure. These results corroborate our previous *operando* study in aqueous proton insertion, which showed that the presence of structural water affords more facile structural transformations, enabling enhanced charge accommodation at faster rates.[12] This facile accommodation of charge density enhances Li^+ storage across a wider potential and temporal range, highlighting the significant impacts of phase-transformation kinetics on electrochemical ion insertion in transition metal oxides.
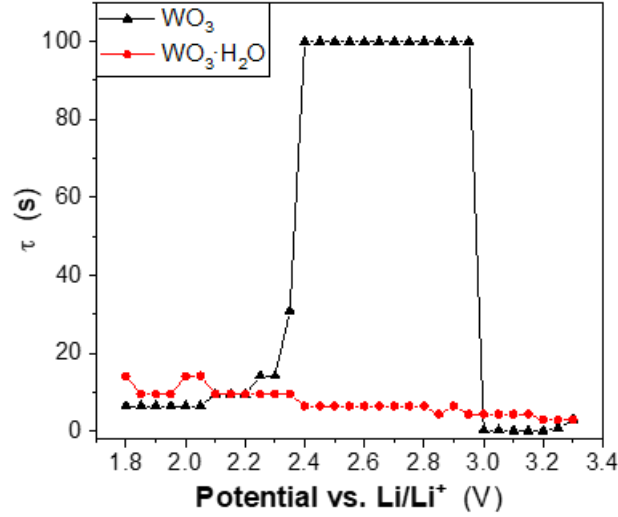
Figure 5: Relaxation Times of WO$_3$•H$_2$O and WO$_3$ | Relaxation times (τ) of WO$_3$•H$_2$O and WO$_3$ as a function of potential. The maximum value of 100 s is limited by the minimum frequency of the measurement (10 mHz), and the true τ values for WO$_3$ between 3.0 and 2.4 V are thus ($\geq$ 100 s).

3D Bode plots, which show both the frequency and potential dependence of *C'* and *C''*,[21] provide a comprehensive picture of the impedance response of the two materials (**Figure 6**). Here, we use the 3D Bode contour plots to summarize the differences in electrochemical Li$^+$ insertion between WO$_3$•H$_2$O and WO$_3$. Overall, WO$_3$•H$_2$O exhibits more significant Li$^+$ storage across a wider potential and temporal range, highlighted by the "waterfall" *C'* behavior. Li$^+$ storage in WO$_3$ occurs over a narrower potential range, and the kinetic limitations of this potential-dependent process lead to more significant capacitance fade at higher frequencies. The enhanced charge transfer and facile structural transformations afforded by the presence of structural water lowers the activation barrier for Li$^+$ insertion, enabling more significant charge storage in finite time and potential ranges.
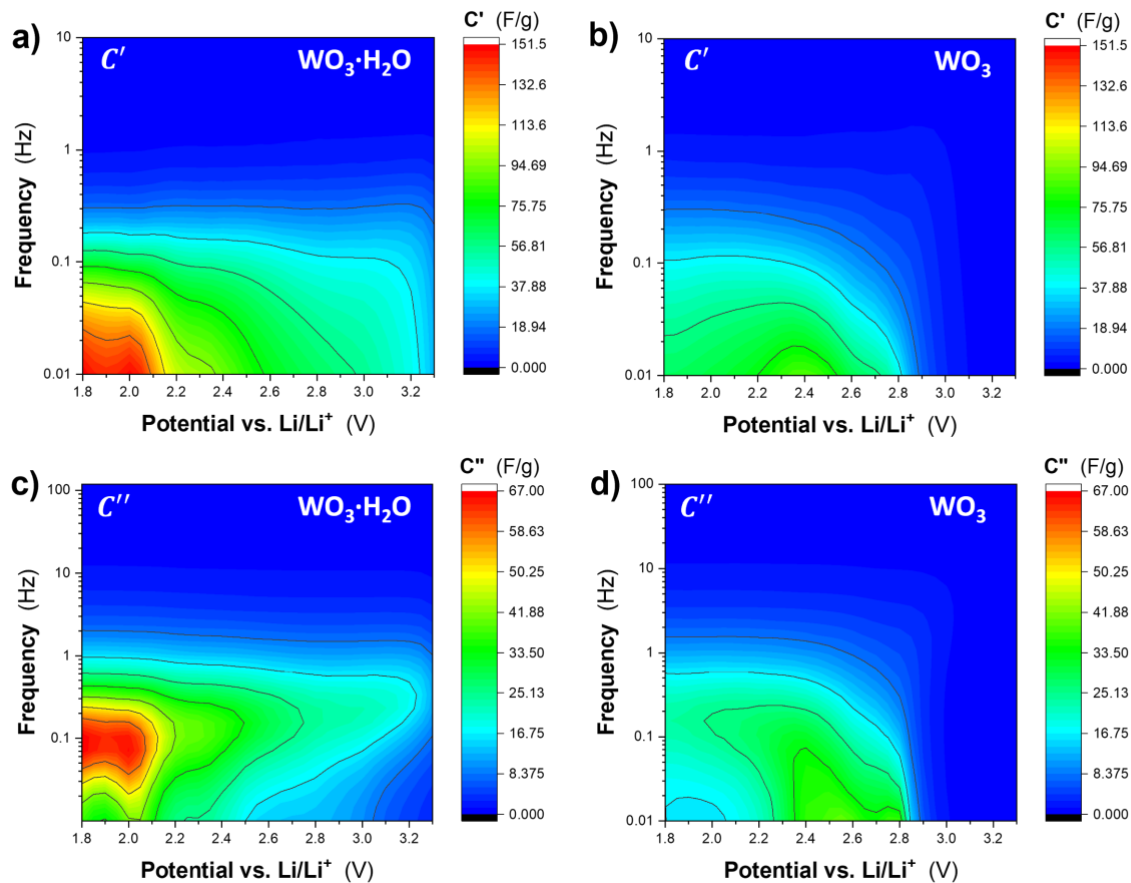
Figure 6: Surface Contour Bode Plot Representations of Li⁺ Charge Storage in WO₃•H₂O and WO₃ | (a, b) *C′* as a function of frequency and potential for WO₃•H₂O and WO₃, respectively and (c, d) *C″* as a function of frequency and potential for WO₃•H₂O and WO₃, respectively.

Conclusions

Understanding the effects of structural water on electrochemical Li⁺ insertion into transition metal oxides will inform materials design strategies for advanced electrochemical technologies. Overall, the presence of structural water in WO₃•H₂O improves Li⁺ insertion kinetics compared to WO₃. *Operando* electrogravimetry and Bode impedance responses of thin-film electrodes were used to probe the kinetic limitations associated with electrochemical

Li$^+$ insertion. EQCM studies reveal negligible solvent co-insertion in both materials. Massograms (Δm vs. ΔE) corroborate the electrochemical responses and indicate that WO_3 undergoes a more potential-dependent Li$^+$ storage process, with a significant portion of its charge storage occurring in a finite potential range. Bode impedance also reveals the difference in the potential-dependent charge storage processes of $WO_3 \bullet H_2O$ and WO_3. The kinetic limitations of this more potential-dependent process hinders the electrode response at faster timescales in WO_3. The thin-film nature of the electrodeposited films lowers solid-state and electrolyte diffusion distances, limiting ion diffusion and electron-transport polarizations. Thus, we hypothesize that the kinetic limitations in WO_3 are due to electrochemically induced structural transformations. Structural water in $WO_3 \bullet H_2O$ leads to more facile structural transformations and thus the Li$^+$ insertion process at fast rates ($t < 10$ min) is not kinetically limited by the nucleation and growth of the Li$^+$-intercalated tetragonal phase. These results are significant because both electrodes possess similar morphologies, undergo the same redox reaction, and were cycled in the same potential window. Designing layered materials with confined fluids that exhibit facile structural transitions may lead to more versatile ion insertion hosts for advanced electrochemical technologies.

References

(1)   Li, M.; Lu, J.; Chen, Z.; Amine, K. 30 Years of Lithium-ion Batteries. *Adv. Mater.* **2018**, *30* (33), 1800561.

(2)   Heo, S.; Dahlman, C. J.; Staller, C. M.; Jiang, T.; Dolocan, A.; Korgel, B. A.; Milliron, D. J. Enhanced Coloration Efficiency of Electrochromic Tungsten Oxide Nanorods by Site Selective Occupation of Sodium Ions. *Nano Lett.* **2020**, *20* (3), 2072–2079.

(3)   Srimuk, P.; Su, X.; Yoon, J.; Aurbach, D.; Presser, V. Charge-Transfer Materials for Electrochemical Water Desalination, Ion Separation and the Recovery of Elements. *Nat. Rev. Mater.* **2020**, 1–22.

(4)   Fuller, E. J.; Li, Y.; Bennet, C.; Keene, S. T.; Melianas, A.; Agarwal, S.; Marinella, M. J.; Salleo, A.; Talin, A. A. Redox Transistors for Neuromorphic Computing. *IBM J. Res. Dev.* **2019**, *63* (6), 1–9.

(5)   Gonzalez-Rosillo, J. C.; Balaish, M.; Hood, Z. D.; Nadkarni, N.; Fraggedakis, D.; Kim, K. J.; Mullin, K. M.; Pfenninger, R.; Bazant, M. Z.; Rupp, J. L. M. Lithium-Battery Anode Gains Additional Functionality for Neuromorphic Computing through Metal–Insulator Phase Separation. *Adv. Mater.* **2020**, *32* (9), 1907465.

(6)   Wise, C. F.; Mayer, J. M. Electrochemically Determined O–H Bond Dissociation Free Energies of NiO Electrodes Predict Proton-Coupled Electron Transfer Reactivity. *J. Am. Chem. Soc.* **2019**, *141* (38), 14971–14975.

(7)   Mizushima, K.; Jones, P. C.; Wiseman, P. J.; Goodenough, J. B. LixCoO2 (0<x⩽1): A New Cathode Material for Batteries of High Energy Density. *Solid State Ionics* **1981**, *3–4*, 171–174.

(8)   Augustyn, V. Tuning the Interlayer of Transition Metal Oxides for Electrochemical Energy Storage. *J. Mater. Res.* **2017**, *32* (1), 2–15.

(9)   Augustyn, V.; Gogotsi, Y. 2D Materials with Nanoconfined Fluids for Electrochemical Energy Storage. *Joule* **2017**, *1*, 443–452.

(10)   Augustyn, V.; Simon, P.; Dunn, B. Pseudocapacitive Oxide Materials for High-Rate Electrochemical Energy Storage. *Energy Environ. Sci.* **2014**, *7*, 1597–1614.

(11)   Park, M.; Zhang, X.; Chung, M.; Less, G. B.; Sastry, A. M. A Review of Conduction Phenomena in Li-Ion Batteries. *J. Power Sources* **2010**, *195* (24), 7904–7929.

(12)   Mitchell, J. B.; Geise, N. R.; Paterson, A. R.; Osti, N. C.; Sun, Y.; Fleischmann, S.; Zhang, R.; Madsen, L. A.; Toney, M. F.; Jiang, D.; Kolesnikov, A. I.; Mamontov, E.; Augustyn, V. Confined Interlayer Water Promotes Structural Stability for High-Rate Electrochemical Proton Intercalation in Tungsten Oxide Hydrates. *ACS Energy Lett.* **2019**, *4* (12), 2805–2812.

(13)   Ji, X.; Chen, J.; Wang, F.; Sun, W.; Ruan, Y.; Miao, L.; Jiang, J.; Wang, C. Water-Activated VOPO4 for Magnesium Ion Batteries. *Nano Lett.* **2018**, *18* (10), 6441–6448.

(14)   Wu, T.; Zhu, K.; Qin, C.; Huang, K. Unraveling the Role of Structural Water in Bilayer V 2 O 5 during Zn 2+-Intercalation: Insights from DFT Calculations. *J. Mater. Chem. A* **2019**, *7* (10), 5612–5620.

(15)   Mitchell, J. B.; Lo, W. C.; Genc, A.; LeBeau, J.; Augustyn, V. Transition from Battery to Pseudocapacitor Behavior via Structural Water in Tungsten Oxide. *Chem. Mater.* **2017**, *29* (9), 3928–3937.

(16)   Wang, R.; Mitchell, J. B.; Gao, Q.; Tsai, W.-Y.; Boyd, S.; Pharr, M.; Balke, N.; Augustyn, V. Operando Atomic Force Microscopy Reveals Mechanics of Structural Water Driven Battery-to-Pseudocapacitor Transition. *ACS Nano* **2018**, *12* (6), 6032–6039.

(17)   Anik, M.; Osseo-Asare, K. Effect of pH on the Anodic Behavior of Tungsten. *J. Electrochem. Soc.* **2002**, *149* (6), B224.

(18)   Babinec, S. J. A Quartz Crystal Microbalance Analysis of Ion Insertion into WO3. *Sol. Energy Mater. Sol. Cells* **1992**, *25* (3), 269–291.

(19)   Bohnke, O.; Vuillemin, B.; Gabrielli, C.; Keddam, M.; Perrot, H.; Takenouti, H.; Torresi,

R. An Electrochemical Quartz Crystal Microbalance Study of Lithium Insertion into Thin Films of Tungsten Trioxide I. Modeling of the Ionic Insertion Mechanism. *Electrochim. Acta* **1995**, *40* (17), 2755–2764.

(20) Razzaghi, F.; Debiemme-Chouvy, C.; Pillier, F.; Perrot, H.; Sel, O. Ion Intercalation Dynamics of Electrosynthesized Mesoporous WO 3 Thin Films Studied by Multi-Scale Coupled Electrogravimetric Methods. *Phys. Chem. Chem. Phys.* **2015**, *17* (22), 14773–14787.

(21) Ko, J. S.; Sassin, M. B.; Rolison, D. R.; Long, J. W. Deconvolving Double-Layer, Pseudocapacitance, and Battery-like Charge-Storage Mechanisms in Nanoscale LiMn2O4 at 3D Carbon Architectures. *Electrochim. Acta* **2018**, *275*, 225–235.

(22) Ko, J. S.; Sassin, M. B.; Parker, J. F.; Rolison, D. R.; Long, J. W. Combining Battery-like and Pseudocapacitive Charge Storage in 3D MnO X@ Carbon Electrode Architectures for Zinc-Ion Cells. *Sustain. Energy Fuels* **2018**, *2* (3), 626–636.

(23) Timofeeva, E. V; Tsirlina, G. A.; Petrii, O. A. Formation of Rechargeable Films on Platinum in Sulfuric Acid Solutions of Isopolytungstates. *Russ. J. Electrochem.* **2003**, *39* (7), 716–726.

(24) Laurinavichute, V. K.; Yu.Vassiliev, S.; Khokhlov, A. A.; Plyasova, L. M.; Molina, I. Y.; Tsirlina, G. A. Electrodeposited Oxotungstate Films: Towards the Molecular Nature of Recharging Processes. *Electrochim. Acta* **2011**, *56* (10), 3530–3536.

(25) Sauerbrey, G. Verwendung von Schwingquarzen Zur Wägung Dünner Schichten Und Zur Mikrowägung. *Zeitschrift für Phys.* **1959**, *155* (2), 206–222.

(26) Wang, R. Ruocun / EQCM. GitHub 2021.

(27) Wang, R.; Chung, C.-C.; Liu, Y.; Jones, J. L.; Augustyn, V. Electrochemical Intercalation of Mg^{2+} into Anhydrous and Hydrated Crystalline Tungsten Oxides. *Langmuir* **2017**, *33* (37), 9314–9323.

(28) Cheng, K. H.; Whittingham, M. S. Lithium Incorporation in Tungsten Oxides. *Solid State Ionics* **1980**, *1* (1–2), 151–161.

(29)   Granqvist, C. G. *Handbook of Inorganic Electrochromic Materials*; Elsevier, 1995.

(30)   Deepa, M.; Srivastava, A. K.; Saxena, T. K.; Agnihotry, S. A. Annealing Induced Microstructural Evolution of Electrodeposited Electrochromic Tungsten Oxide Films. *Appl. Surf. Sci.* **2005**, *252* (5), 1568–1580.

(31)   Nikitina, V. A.; Vassiliev, S. Y.; Stevenson, K. J. Metal-Ion Coupled Electron Transfer Kinetics in Intercalation-Based Transition Metal Oxides. *Adv. Energy Mater.* **2020**, *10* (22), 1903933.

(32)   Granqvist, C. G. Tungsten Oxide Films: Ion Intercalation/deintercalation Studied by Physical Techniques. In *Handbook of Inorganic Electrochromic Materials*; Elsevier, Ed.; Amsterdam, 2002; pp 111–137.

(33)   Nishiyama, K.; Sasano, J.; Yokoyama, S.; Izaki, M. Electrochemical Preparation of Tungsten Oxide Hydrate Films with Controlled Bandgap Energy. *Thin Solid Films* **2017**, *625*, 29–34.

(34)   Wen, R.-T.; Granqvist, C. G.; Niklasson, G. A. Eliminating Degradation and Uncovering Ion-Trapping Dynamics in Electrochromic WO 3 Thin Films. *Nat. Mater.* **2015**, *14* (10), 996–1001.

(35)   Judeinstein, P.; Livage, J. Role of the Water Content on the Electrochromic Properties of $WO_3 \cdot nH_2O$ Thin Films. *Mater. Sci. Eng. B3* **1989**, *3*, 129–132.

(36)   Tsai, W.-Y.; Taberna, P.-L.; Simon, P. Electrochemical Quartz Crystal Microbalance (EQCM) Study of Ion Dynamics in Nanoporous Carbons. *J. Am. Chem. Soc.* **2014**, *136* (24), 8722–8728.

(37)   Seidl, L.; Bucher, N.; Chu, E.; Hartung, S.; Martens, S.; Schneider, O.; Stimming, U. Intercalation of Solvated Na-Ions into Graphite. *Energy Environ. Sci.* **2017**, *10* (7), 1631–1642.

(38)   Levi, M. D.; Lukatskaya, M. R.; Sigalov, S.; Beidaghi, M.; Shpigel, N.; Daikhin, L.; Aurbach, D.; Barsoum, M. W.; Gogotsi, Y. Solving the Capacitive Paradox of 2D MXene Using Electrochemical Quartz-crystal Admittance and in Situ Electronic Conductance

Measurements. *Adv. Energy Mater.* **2015**, *5* (1), 1400815.

(39)   Levi, M. D.; Shpigel, N.; Sigalov, S.; Dargel, V.; Daikhin, L.; Aurbach, D. In Situ Porous

Structure Characterization of Electrodes for Energy Storage and Conversion by EQCM-

D: A Review. *Electrochim. Acta* **2017**, *232*, 271–284.

(40)   Xu, K. "Charge-Transfer" Process at Graphite/electrolyte Interface and the Solvation

Sheath Structure of Li+ in Nonaqueous Electrolytes. *J. Electrochem. Soc.* **2007**, *154*

(3), A162.

(41)   Shouji, E.; Buttry, D. A. {EQCM} Measurements of Solvent Transport during Li+

Intercalation in {V2O5} Xerogel Films. *Electrochim. Acta* **2000**, *45* (22–23), 3757–3764.

(42)   Wang, R.; Boyd, S.; Bonnesen, P. V; Augustyn, V. Effect of Water in a Non-Aqueous

Electrolyte on Electrochemical Mg2+ Insertion into WO3. *J. Power Sources* **2020**, *477*,

229015.

(43)   Taberna, P. L.; Simon, P.; Fauvarque, J.-F. Electrochemical Characteristics and

Impedance Spectroscopy Studies of Carbon-Carbon Supercapacitors. *J. Electrochem.*

Soc. **2003**, *150* (3), A292.

(44)   Banda, H.; Périé, S.; Daffos, B.; Dubois, L.; Crosnier, O.; Simon, P.; Taberna, P.-L.;

Duclairoir, F. Investigation of Ion Transport in Chemically Tuned Pillared Graphene

Materials through Electrochemical Impedance Analysis. *Electrochim. Acta* **2019**, *296*,

882–890.

(45)   Banda, H.; Périé, S.; Daffos, B.; Taberna, P.-L.; Dubois, L.; Crosnier, O.; Simon, P.; Lee,

D.; De Paëpe, G.; Duclairoir, F. Sparsely Pillared Graphene Materials for High-

Performance Supercapacitors: Improving Ion Transport and Storage Capacity. *ACS*

Nano **2019**, *13* (2), 1443–1453.

(46)   Zhong, Q.; Dahn, J. R.; Colbow, K. Lithium Intercalation into WO_3 and the Phase

Diagram of Li_xWO_3. *Phys. Rev. B* **1992**, *46* (4), 2554–2560.